CONDENSED MATTER PHYSICS

Unusual charge density wave introduced by the Janus structure in monolayer vanadium dichalcogenides

Ziqiang Xu[1]†, Yan Shao[1]†, Chun Huang[1]†, Chao Zhu[2]†, Genyu Hu[1], Shihao Hu[1], Zhi-Lin Li[3], Xiaoyu Hao[1], Yanhui Hou[1], Teng Zhang[1], Liwei Liu[1], Jin-An Shi[3], Chen Liu[4], Jia-Ou Wang[4], Wu Zhou[3], Jiadong Zhou[1], Wei Ji[5], Yeliang Wang[1]*, Chendong Zhang[2]*, Jingsi Qiao[1]*, Hong-Jun Gao[3], Xu Wu[1]*

As a fundamental structural feature, the symmetry of materials determines the exotic quantum properties in transition metal dichalcogenides (TMDs) with charge density waves (CDWs). The Janus structure, an artificially constructed lattice, provides an opportunity to tune the electronic structures and their associated behavior, such as CDW states. However, limited by the difficulties in atomic-level fabrication and material stability, the experimental visualization of the CDW states in two-dimensional (2D) TMDs with Janus structure is still rare. Here, using surface selenization of VTe_2, we fabricated monolayer Janus VTeSe. With scanning tunneling microscopy, we observed and characterized an unusual $\sqrt{13} \times \sqrt{13}$ CDW state with threefold rotational symmetry breaking. Combined with theoretical calculations, we find that this CDW state can be attributed to the magnetic-involved charge modulation in the Janus VTeSe, rather than the conventional electron-phonon coupling. Our findings provide a promising platform for studying the CDW states and artificially tuning the electronic properties of the 2D TMDs toward the related fundamental and applied studies.

INTRODUCTION

Symmetry, a fundamental feature, plays an important role in determining the properties of materials. As a collective excitation of atomic lattices, the charge density wave (CDW) transition modulates the symmetry and the electron density, especially for cases with unusual order. In electron-correlated two-dimensional (2D) transition metal dichalcogenides (TMDs), the CDW states always exist and are associated with their exotic quantum properties, such as Mott insulating, spin density wave, 2D magnetism, and unconventional superconductivity (*1*–*12*). Thus, manipulating the symmetry of the lattice and the CDW states, such as breaking the rotational symmetry, offers extraordinary opportunities to tune their many-body ground states to introduce unique physics and applications (*13*–*20*). Breaking the lattice inversion symmetry and tuning the lattice constant, the Janus structure, an artificially constructed lattice, provides unprecedented possibilities to tune electronic states by engineering structural characteristics. Recently, Janus structures have been realized on semiconducting 2D TMDs and brought distinct properties such as strong Rashba spin splitting and enhanced piezoelectric effect (*21*–*24*). However, limited by both their fabrication controllability and stability, the metallic 2D TMDs with the Janus structure and their CDW states are rarely studied, leaving only a few theoretical predictions (*25*, *26*).

As representative members in metallic TMDs, vanadium dichalcogenides (VX_2, X = S, Se, and Te) always own CDW states. They are expected to host plentiful structures with exotic properties, such as the in-plane anomalous Hall effect in the VS_2-VS superlattice with symmetry breaking, as reported in our previous work (*27*). Associated with the debatable 2D magnetic properties, 2D VX_2 systems show distinct layer-dependent CDW states with reducing dimensionality (*28*–*32*). Specifically, the monolayer VS_2 and VSe_2 show various CDW superlattices with rotational symmetry breaking, such as $\sqrt{7} \times \sqrt{3}$ (*32*, *33*), while the monolayer VTe_2 owns a modulated 4×4 CDW order, following the symmetry of its Bragg lattice (*34*, *35*). These CDW states with different periods and symmetries imply that multiple driven forces may contribute to the formation of CDW, in addition to the conventional electron-phonon coupling. Introducing the Janus structure is expected to artificially change the structural characteristics and the corresponding band structure of the 2D vanadium dichalcogenides, providing a promising platform for investigating the CDW states.

In this paper, we report the unusual CDW states with rotation symmetry breaking in artificial monolayer Janus VTeSe (J-VTeSe). By atomic-scale selenization of top-layer Te atoms in monolayer VTe_2, we fabricated J-VTeSe and determined its Janus structure using x-ray photoelectron spectroscopy (XPS) and scanning transmission electron microscopy (STEM). Then, scanning tunneling microscopy/spectroscopy (STM/STS) characterized a rhombic $\sqrt{13} \times \sqrt{13}$ CDW state in atomic scale. The energy- and spatial-resolved STS results reveal the distinct and complicated orbital texture near the Fermi energy of monolayer J-VTeSe. Combined with density functional theory (DFT) calculations, we suggest that the $\sqrt{13} \times \sqrt{13}$ CDW state in the J-VTeSe can be attributed to the magnetic-involved charge modulation, rather than the conventional electron-phonon coupling. With the atomically controllable surface selenization, our work provides a technique for introducing the Janus structure into TMDs and observing the associated CDW states in atomic scale. Precisely tuning the

[1]State Key Laboratory of Chips and Systems for Advanced Light Field Display, Center for Interdisciplinary Science of Optical Quantum and NEMS Integration, School of Physics, School of Interdisciplinary Science, and School of Integrated Circuits and Electronics, Beijing Institute of Technology, Beijing 100081, China. [2]School of Physics and Technology, Wuhan University, Wuhan 430072, China. [3]Institute of Physics and University of Chinese Academy of Sciences, Chinese Academy of Sciences, Beijing 100190, China. [4]Institute of High Energy Physics, Chinese Academy of Sciences, Beijing 100049, China. [5]Beijing Key Laboratory of Optoelectronic Functional Materials and Micro-Nano Devices, Department of Physics, Renmin University of China, Beijing 100872, China.
*Corresponding author. Email: yeliang.wang@bit.edu.cn (Y.W.); cdzhang@whu.edu.cn (C.Z.); qiaojs@bit.edu.cn (J.Q.); xuwu@bit.edu.cn (X.W.)
†These authors contributed equally to this work.

atomic lattice constant, this Janus-structure fabrication method shows the potential to tune the electronic properties toward their future fundamental and applied studies.

RESULTS

Fabrication of monolayer J-VTeSe

The J-VTeSe sample was fabricated by atomic-scale surface selenization of monolayer VTe_2, as shown by the schematic in Fig. 1A. We prepared monolayer VTe_2 on the bilayer graphene/SiC (0001) substrate (left panel). Then, the surface selenization process was performed by depositing Se onto the monolayer VTe_2, which was kept at ~523 K. After the selenization process, the region with J-VTeSe is formed (right panel), and the ratio of this region can be increased by lengthening the selenization time, which can be attributed to Se atoms gradually substituting top-layer Te atoms of the VTe_2 structure.

To characterize the selenization of monolayer VTe_2, we performed the in situ XPS measurements on the as-prepared and selenized VTe_2 samples, respectively. As shown in Fig. 1B (see figs. S1 and S2 for more information), the doublet peaks originating from the V $2p_{1/2}$ and $2p_{3/2}$ core levels of the as-prepared VTe_2 structure (colored blue) are located at 519.93 and 512.41 eV, respectively. After selenization for 30, 60, and 360 min, the peaks shift to higher binding energy at 520.23/512.60, 520.27/512.74, and 520.40/512.81 eV, respectively. Combined with the XPS results of VSe_2 (*30*), the energy shift of ~0.40 eV of the selenized VTe_2 confirms the selenization and indicates the change of the gradual structural transformation. In addition, the doublet peaks originating from the Te 3d and Se 3d core levels of the selenized sample both show an energy shift of ~0.10 eV compared to the intrinsic VTe_2 and VSe_2, respectively. The uniform energy shift of the selenized sample also indicates the changes in chemical states after the selenization (fig. S3), though the value is close to the energetic resolution.

Characterizing atomic structure of monolayer vanadium dichalcogenides

To determine the atomic structure of the selenized vanadium dichalcogenides sample in atomic scale, we conducted STEM measurements

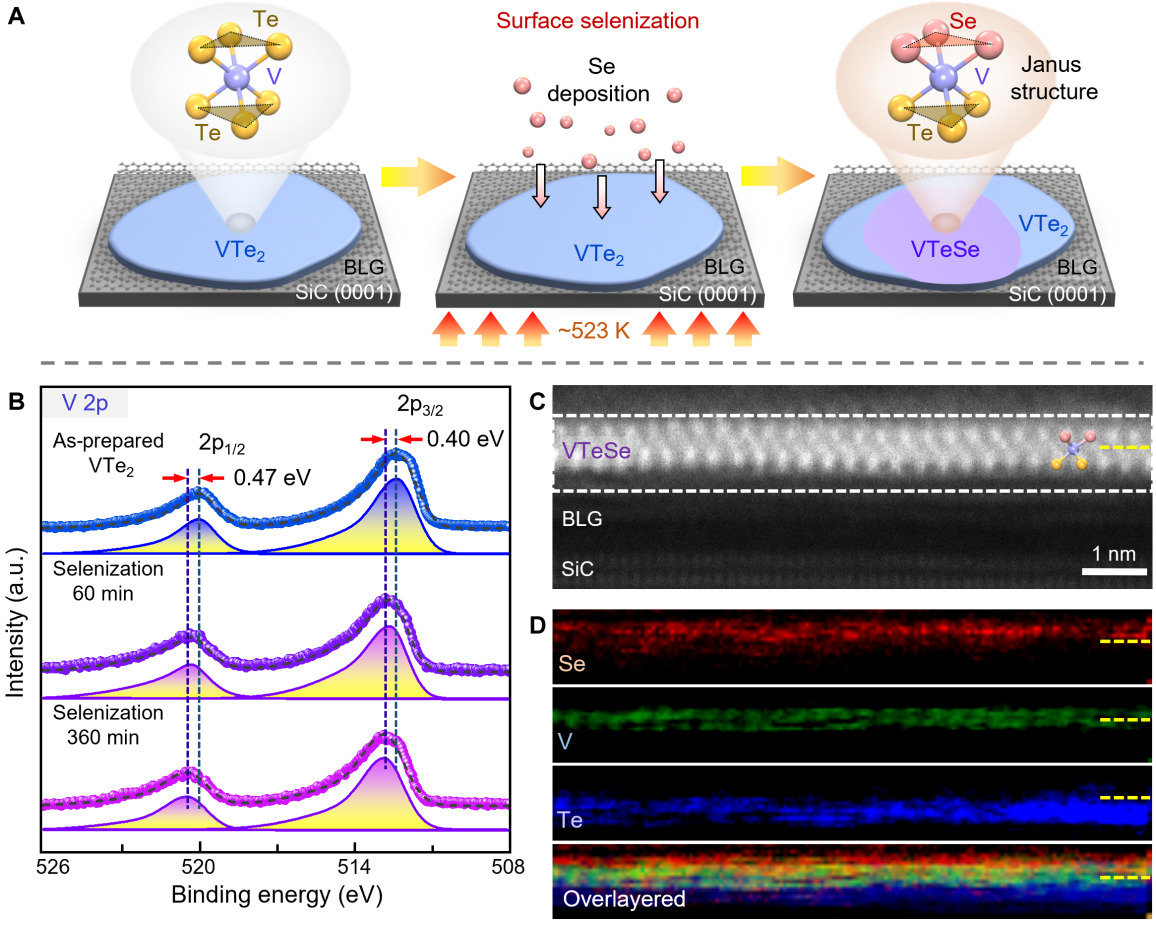

Fig. 1. Fabrication of the monolayer J-VTeSe. (**A**) The schematic of the synthesis process. The monolayer J-VTeSe is fabricated by surface selenization of monolayer VTe_2. (**B**) XPS results of V 2p spectra of the sample during the selenization process. The V 2p peak positions (of as-prepared VTe_2 at 519.93 and 512.41 eV, of the sample with 60 min selenization at 520.27 and 512.74 eV, and of the sample with 360 min of selenization at 520.40 and 512.81 eV) show apparent energy differences before and after selenization. (**C**) ADF STEM image of the sample cross section, showing the sandwich-like 1T structure of the J-VTeSe monolayer with top Se (red), bottom Te (yellow), and middle V (blue) atoms. (**D**) The corresponding EELS maps of the dashed frame in (C). The layers of Se, Te, and V are colored red, blue, and green, respectively. The yellow dashed lines mark the position of the V layer in each EELS map.

on the samples selenized for 60 min. The large-scale bright-field and dark-field cross-sectional images (fig. S4) demonstrate a well-ordered sandwich-like structure (*36*). As marked by the model, a typical 1T structure was confirmed by the zoomed-in annular dark-field (ADF) STEM results, as shown in Fig. 1C. Moreover, the element information of atoms can be further distinguished by the corresponding real-space atomic resolution electron energy-loss spectroscopy (EELS) elemental map (Fig. 1D). Unambiguously, the results demonstrate that the sandwich-like structure, from top to bottom, consists of Se, V, and Te atoms with one atomic-layer thickness, as colored by red, green, and blue, respectively. Therefore, we can confirm that the J-VTeSe has been fabricated by direct selenization of monolayer VTe_2 with atomic-level control.

Following the atomic characterization in the side view, we performed STM measurements to visualize the top-view atomic structure. STM images of the samples with different selenization times were taken at room temperature (fig. S5). Without CDW superlattice, the atomic-resolution STM images on different regions reveal the close-packed structure. The lattice constant difference between VTe_2 and J-VTeSe is very small, which is 0.36 ± 0.01 and 0.35 ± 0.01 nm, corresponding to VTe_2 and J-VTeSe, respectively. To further characterize the atomic structure, low-temperature (LT)–STM measurements (4.5 K) were performed on the sample selenized for 60 min. In Fig. 2A, we can see two kinds of regions of the sample, and the height difference is ~0.06 ± 0.03 nm, according to the height profile in Fig. 2B. The height difference between VTe_2 and J-VTeSe follows their atomic models. Unlike the results of room-temperature STM, the J-VTeSe demonstrates a distinct superlattice from VTe_2 in the LT-STM image (fig. S6), which could be attributed to the CDW orders (*34*, *35*).

Atomic structure and electronic states of CDW

To investigate the CDW states, we obtained atomic-resolution STM images of monolayer VTe_2 and J-VTeSe, using LT-STM at 4.5 K. As shown in Fig. 2C, a typical CDW superstructure with threefold rotational symmetry can be observed in the monolayer VTe_2. The STM image indicates a 4 × 4 CDW order with the lattice constant $\mathbf{a}_{cdw}$ = 1.42 nm (marked as black arrows), consistent with previous reports (*35*). Having threefold symmetry, two sets of spots can be observed in the corresponding fast Fourier transform (FFT) pattern (shown in Fig. 2C, inset). The outer six spots represent the Bragg lattice of VTe_2 (black circles), and the inner six spots represent the

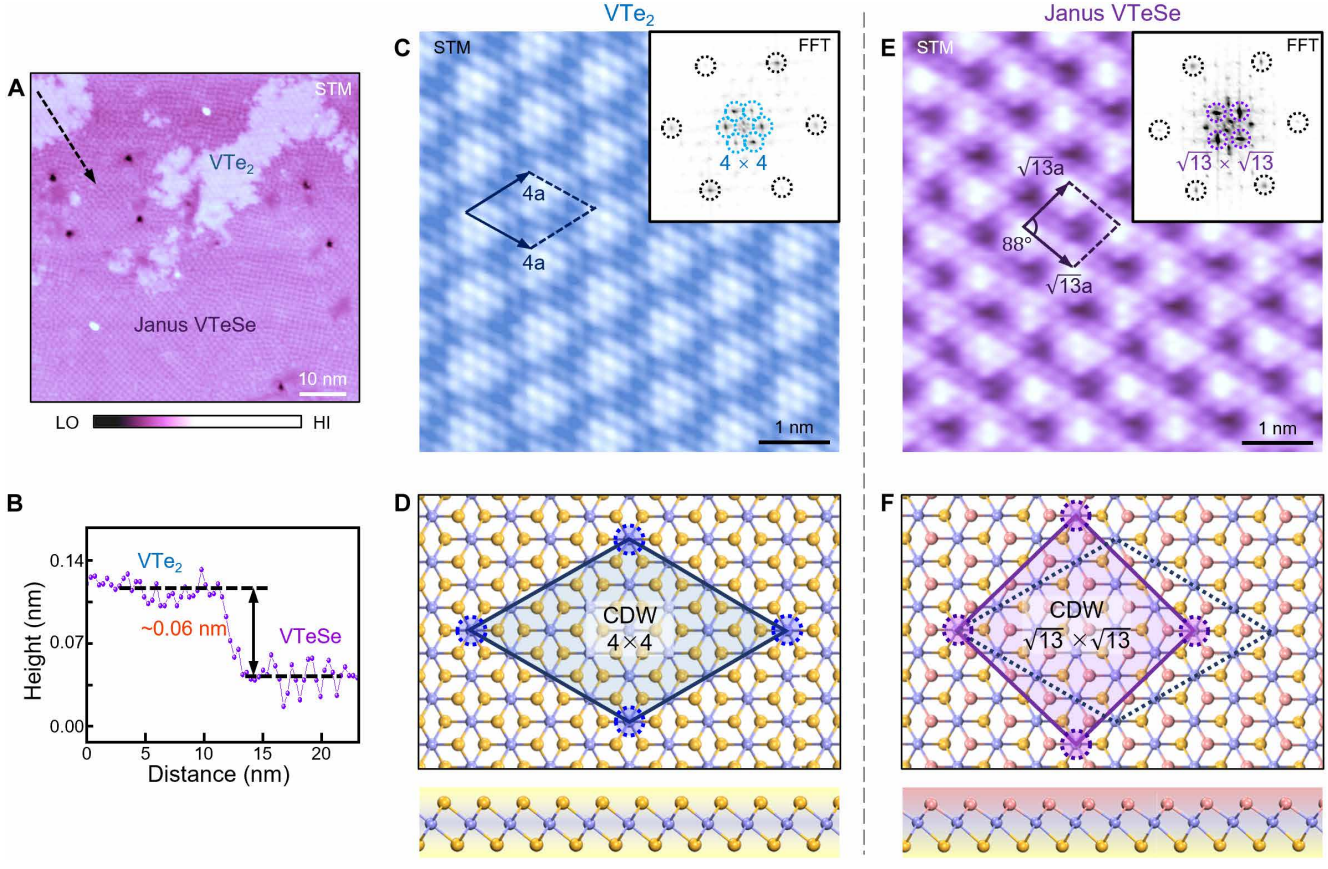

Fig. 2. Atomic structure of monolayer V dichalcogenides. (**A**) Typical STM image taken at ~4.5 K after sample with 60 min of selenization. (**B**) The corresponding height profile along the black arrow in (A), indicating the height difference between the VTe_2 and J-VTeSe. (**C** and **E**) The atomic-resolution STM images of the monolayer VTe_2 (C) and J-VTeSe (E), respectively. The unit cells of the CDW superstructure of VTe_2 and J-VTeSe are marked by black rhomboids, respectively. Inset: The corresponding FFT patterns, verifying the 4 × 4 CDW superlattice in VTe_2 (C) and the $\sqrt{13} \times \sqrt{13}$ CDW superlattice in J-VTeSe (E), respectively. (**D** and **F**) Corresponding atomic models of VTe_2 (D) and J-VTeSe (F) structures in top views (top) and side views (bottom). The Se, Te, and V atoms are represented as red, yellow, and blue balls, respectively. The unit cells of the two CDW superlattices are marked and shaded for better comparison. STM parameters: Sample bias U = −1.0 V, Setpoint I = 10 pA (A); U = −0.3 V, I = 100 pA [(C) and (E)].

CDW lattice (cyan circles), indicating the hexagonal 4 × 4 CDW superstructure.

Distinct from VTe_2, J-VTeSe owns a rhombic $\sqrt{13} \times \sqrt{13}$ CDW order with threefold rotation symmetry breaking, as shown in Fig. 2E. The unit cell of the superlattice is marked by the black rhombus with the lattice constant $\mathbf{a}_{cdw} = 1.26 \pm 0.03$ nm ($\sqrt{13} \times a_{VTeSe} = 1.26$ nm). Moreover, the rhombic $\sqrt{13} \times \sqrt{13}$ has an angle between the two basic vectors of ~88°, which is distinct from the well-known "star-of-David" $\sqrt{13} \times \sqrt{13}$ R13.9° superlattice (*11*, *12*). From the corresponding FFT pattern (as inset), we can identify six spots of the J-VTeSe Bragg lattice (black circles), which are similar to VTe_2. Unlike the results of VTe_2, it shows another four spots in the pattern of J-VTeSe, indicating the rhombic CDW superlattice (purple circles). These FFT spots further verify the rhombic $\sqrt{13} \times \sqrt{13}$ CDW orders.

Considering the CDW superlattice of VTe_2 and J-VTeSe, the corresponding atomic models can be labeled, as shown in Fig. 2 (D and F). Compared with the 4 × 4 CDW order of VTe_2, the $\sqrt{13} \times \sqrt{13}$ CDW superlattice in J-VTeSe could be regarded as the two basic vectors rotating outward for ~14°. The terminal of the $\sqrt{13} \times \sqrt{13}$ basic vectors can be considered as those of the 4 × 4 superlattice moving for 1 unit cell along the atomic lattice as shown by the rhombuses in Fig. 2F. Then, each $\sqrt{13} \times \sqrt{13}$ unit cell owns 15 V atoms, which is 1 atom less than the 4 × 4 unit cell. It is worth noting that the $\sqrt{13} \times \sqrt{13}$ CDW of J-VTeSe is different from the star-of-David $\sqrt{13} \times \sqrt{13}$ CDW order in $TaSe_2$ or $NbSe_2$, though both of them own the same V atom number, the latter of which still keeps the threefold symmetry (*9*–*12*). As a result, it formed an unusual CDW order with twofold symmetry instead of the threefold symmetry 4 × 4 CDW order of VTe_2, implying that other driving forces should contribute to the CDW formation. Besides, according to the varying temperature STM results (figs. S7 and S8), the CDW order can transfer to 4 × 4 at the temperature above 78 K and disappear at the critical temperature of ~190 K.

To investigate the electronic structure of the CDW state, we performed energy- and spatial-resolved STS measurements to study the electronic local density of states (LDOS) of J-VTeSe. The typical d*I*/d*V* spectra taken on VTe_2 and J-VTeSe, respectively, are shown in Fig. 3A (top panel). Both spectra indicate the CDW gap at the Fermi level, appearing as a wide dip with a finite value at its minimum. Besides the CDW gap, the big peaks contributed by the *d* orbital of V atoms show the position at ~−100 meV for VTe_2 and ~+60 meV for J-VTeSe. To gain additional insight into the CDW states at different energies, we performed d*I*/d*V* spatial mapping of J-VTeSe at different bias voltages near Fermi energy (E_F), as shown in Fig. 3 (B to F) (see figs. S9 and S10 for more information), indicating the energy-dependent orbital textures. Considering the tip-induced switch of the CDW state in high bias scanning (fig. S11), we did the

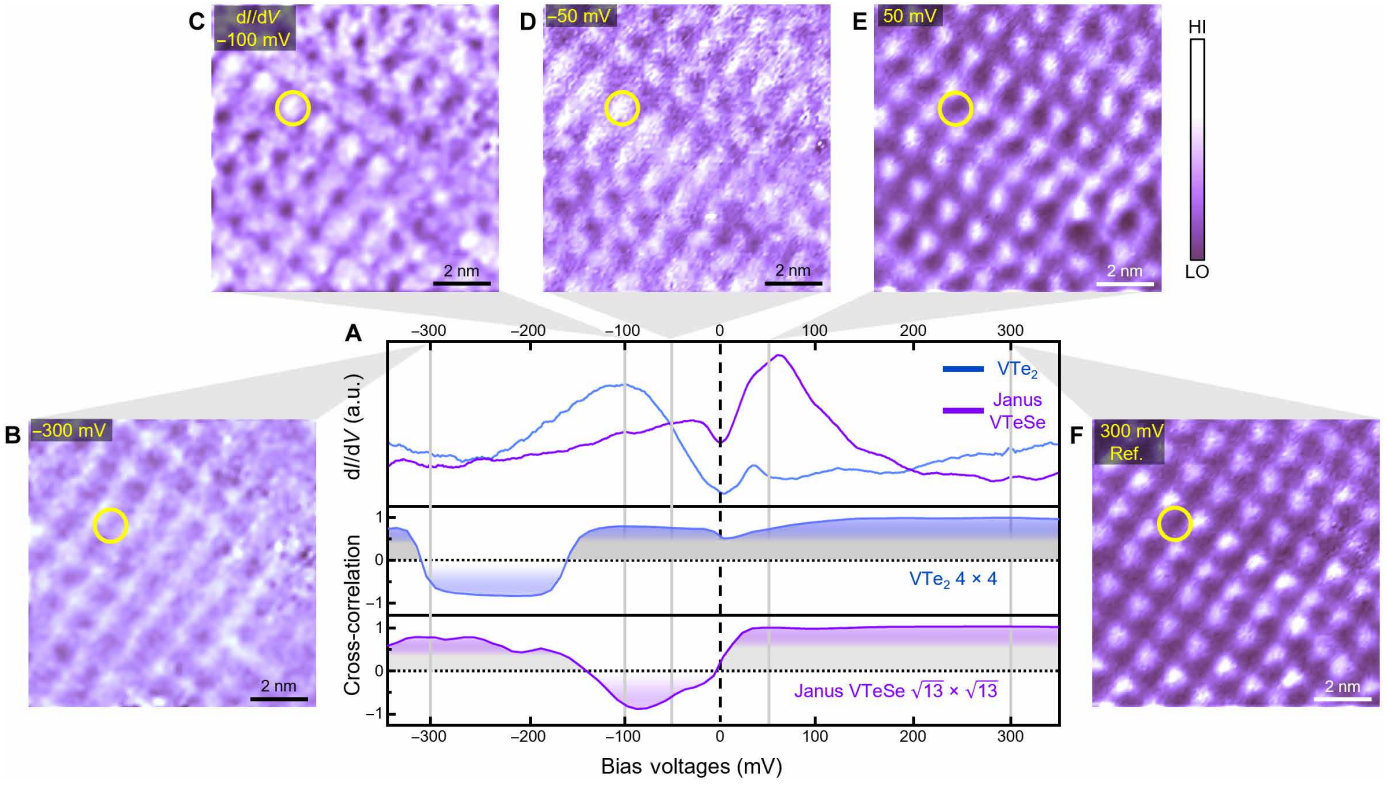

Fig. 3. Energy- and spatial-resolved STS results of the unusual CDW state in monolayer J-VTeSe. (**A**) Top: The STM d*I*/d*V* spectra of the monolayer VTe_2 and J-VTeSe, respectively. They show the CDW gap and the electronic states near the Fermi level. Middle and bottom: The cross-correlation curves of d*I*/d*V* maps of both VTe_2 (middle) and J-VTeSe (bottom) at different energies, with the reference map taken at 300 mV [shown in fig. S9 and (F)], respectively. (**B** to **F**) Constant-height d*I*/d*V* conductance maps taken at selected bias voltages. The same area is marked with yellow circles on each map. STM d*I*/d*V* parameters: modulation voltage $V_{r.m.s.} = 10$ mV, frequency $f = 973$ Hz, stabilization position, $U = -0.35$ V, $I = 50$ pA.

STS mapping at the bias from −350 to 350 mV with a step of 10 mV. The mappings measured at different biases show distinct features, especially for those taken on the energy below and above Fermi energy. As marked by the yellow circles, we can see that the contrast inversion appears at the mapping at −100 and 50 meV (C and E), which indicates the superlattice origin from CDW transitions.

To further quantify the energy-dependent LDOS distribution of VTe_2 and J-VTeSe, we cross-correlated our dI/dV maps with a reference map taken at +300 meV of the conduction band (*11*). The resulting normalized cross-correlation values of both VTe_2 and J-VTeSe as a function of bias voltages are color coded in the bottom panel of Fig. 3A. The conduction band ($V > 0$ V) of both VTe_2 and J-VTeSe has a strong and positive cross-correlation (close to 1, gray). It means that the orbital texture remains almost unchanged at the conduction band for both VTe_2 and J-VTeSe.

At the energy of the valence band ($V < 0$ V), the normalized cross-correlation curves show different features between VTe_2 and J-VTeSe. The dI/dV mappings of VTe_2 at the energy between −300 and −200 meV are strongly anticorrelated with the conduction band map, while it flips to positive at −150 meV, which is still far from the Fermi energy. For the J-VTeSe, the mappings are partially anticorrelated at the energy between −100 and 0 meV with the conduction band map. Specifically, it flips to the positive cross-correlation at the Fermi energy. Moreover, compared with the smooth curve of VTe_2, the normalized cross-correlation curve of J-VTeSe is fluctuant, which indicates the complicated orbital texture. With the combination of the rotation symmetry breaking and the unique orbital texture, we can see that the mechanism of the CDW state in J-VTeSe is beyond the simple conventional Peierls description, which induces the CDW state in VTe_2, and should be associated with another mechanism (*37*).

DFT calculation results of monolayer J-VTeSe

Previous studies indicated that magnetic ordering plays an important role in the structure and stability of the VX_2 (X = Se and Te) systems (*28*, *29*). Therefore, to investigate the mechanism of the J-VTeSe CDW states, DFT calculations were performed considering the magnetic order, including nonmagnetic (NM), ferromagnetic (FM), and two antiferromagnetic orders (AFM-stripe and AFM-zigzag), as shown in Fig. 4A. With the corresponding atomic configurations, the supercells for the calculation are $2 \times \sqrt{3}$ for the pristine state and 4×4 and $\sqrt{13} \times \sqrt{13}$ for the CDW states, considering the experimental results (Fig. 2F). As the basic structure, the band structure of the NM on the Fermi level reveals that the Fermi nesting vector is $q = 0.25\ a^*$, similar to the calculation results of VSe_2 and VTe_2 (fig. S12 and table S1). Besides, the phonon dispersion calculation results of the NM show the lowest imaginary frequencies located at q point (0.25, 0, 0), as shown in Fig. 4C (*38*–*40*). It would lead to a 4×4 CDW order, with the typical threefold symmetry. The mechanism for the symmetry breaking of the CDW order is still unsolved by conventional Fermi surface nesting and electron-phonon coupling, though the unconventional $\sqrt{13} \times \sqrt{13}$ CDW order can be achieved by introducing small perturbation in 4×4 supercells.

Furthermore, the calculations with the various magnetic orders were performed. As revealed by the relative energy in Fig. 4D, the FM and AFM orders exhibit unambiguous lower energies, compared with the NM results for all the atomic configurations. Moreover, the AFM orders, including AFM-stripe and AFM-zigzag, own similar energies and are more stable than the structures with FM orders. Compared to NM structures, magnetic orders, especially the AFM-stripe and AFM-zigzag, exhibit lattice expansion and induce C_3 rotational symmetry breaking with 1 to 3% differences in lattice constants a and b (fig. S13 and table S2). Besides, the introduction of spin also disturbed the nesting vector (fig. S14). Combined with the more complicated phonon dispersions of the AFM structures (fig. S15), it reveals that the magnetic order affects the typical NM electron-phonon coupling in the formation of CDW order.

For the $\sqrt{13} \times \sqrt{13}$ CDW order, STM simulations with the energy range of [−0.5, 0] eV show that the result of the AFM-stripe structure matches better with the experimental images than the AFM-zigzag (fig. S16), despite the slightly low energy of the latter. It also lowers the density of states at the Fermi surface, compared with those of the pristine structure with the same AFM-stripe order as shown in Fig. 4F. Considering the temperature-dependent experimental results, we also performed the corresponding calculation and the STM simulation with the 4×4 CDW order. From the results (figs. S17 and S18), we can see that the simulation image of the AFM-zigzag and NM matches well with the experimental results in the 4×4 CDW, instead of the AFM-stripe for the $\sqrt{13} \times \sqrt{13}$ CDW order. These results imply that a magnetic order transition appears below the CDW critical temperature, which is consistent with the two transitions in the experimental results. Thus, we can see that the symmetry breaking of the VTeSe CDW order can be attributed to the charge modulation originating from the combination of the electron, magnetism, and phonon. With the lattice intermediate of the VTe_2 and VSe_2, the J-VTeSe shows a locally uniform and temperature-tunable CDW order, which would be different from the simple solid solution of Se in VTe_2.

DISCUSSION

In summary, we have introduced the Janus structure into 2D vanadium dichalcogenides and artificially fabricated J-VTeSe by atomic-scale direct selenization. Through various atomic-level characterization methods, we confirmed the atomic structure of J-VTeSe and its emerged CDW order with threefold rotation symmetry breaking. The experimental spectroscopic imaging reveals an unusual and complicated orbital texture near Fermi energy. From the theoretical calculations with the magnetic orders, we found that magnetic-involved charge modulation supplements the conventional electron-phonon coupling mechanism and affects the CDW formation of the 2D vanadium dichalcogenides. With the combination of the precise modification of lattice constant and structure sensitivity of the magnetic order, the Janus structure and the rotational symmetry breaking of CDW states can be associated in 2D TMDs. Our findings also provide an effective method to artificially construct the Janus structures in TMDs and tune their electronic properties.

MATERIALS AND METHODS

Sample preparation

Monolayer VTe_2 was epitaxially grown on bilayer graphene/SiC (0001) substrate in an ultrahigh vacuum (UHV) chamber, with a base pressure of 2×10^{-10} mbar, equipped with standard molecular beam epitaxy capabilities. The bilayer graphene/SiC (0001) substrate

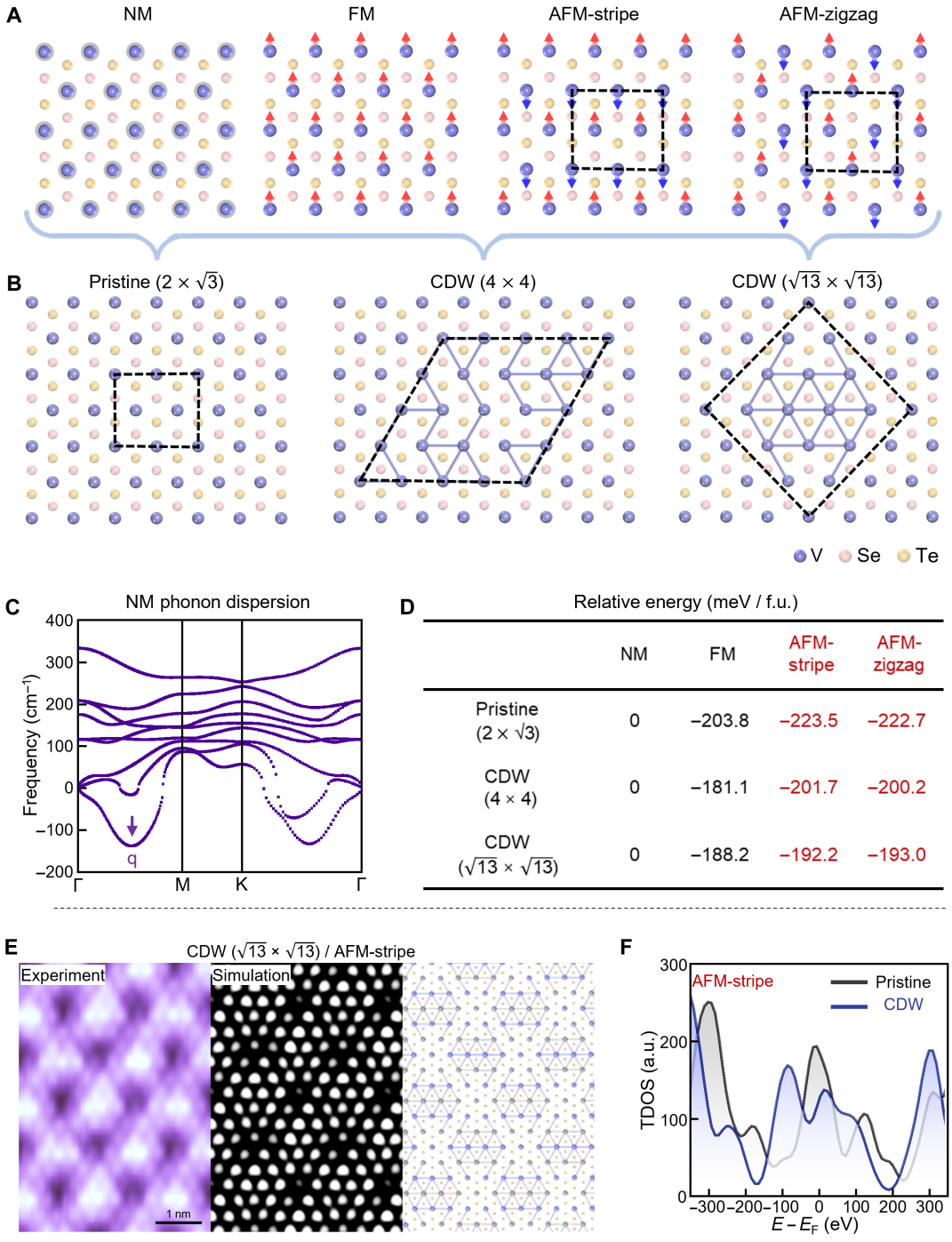

Fig. 4. The theoretical calculations of the monolayer J-VTeSe. (**A**) The ball-and stick schematics of the nonmagnetic (NM), ferromagnetic (FM), and antiferromagnetic (AFM-stripe and AFM-zigzag) orders of the J-VTeSe. The spin textures are depicted with red and blue arrows. (**B**) The ball-and stick schematics of the pristine, CDW (4 × 4), and CDW ($\sqrt{13} \times \sqrt{13}$) configurations. Dashed lines in (A) and (B) correspond to the supercells. The purple sticks represent the shortened atomic distances between two adjacent V atoms. (**C**) Phonon dispersions of NM pristine J-VTeSe at 1.17 K. The lowest imaginary frequency (marked by a purple arrow) is located at the q = (0.25, 0, 0) point. (**D**) Relative energy comparison of four magnetic configurations, normalized to the NM one (set as 0 eV). (**E**) The comparison of the STM images (left), simulation (middle), and atomic schematic (right) of the CDW J-VTeSe with AFM-stripe order and CDW ($\sqrt{13} \times \sqrt{13}$) configuration. The energy range of the simulation is [−0.1, 0] eV. (**F**) Density of states of $\sqrt{13} \times \sqrt{13}$ AFM-S CDW and pristine J-VTeSe.

was prepared by annealing the doped SiC crystalline substrate (TankeBlue) at 1500 K for 180 min after degassing at 900 K for 5 hours. Tellurium clusters (Sigma, 99.999%) were evaporated from a Knudsen cell, vanadium atoms (ESPI Metals, 99.999%) were evaporated from an electron-beam evaporator, and they were deposited onto the bilayer graphene/SiC (0001) substrate, kept at 550 K. The growth parameters were under Te-rich conditions, aiming to guarantee that there are enough Te atoms involved in the reaction with vanadium. The excessive tellurium atoms will be desorbed from the substrate because the substrate temperature at 550 K was higher than the evaporation temperature of tellurium atoms (520 K). For the fabrication of J-VTeSe, selenium clusters (Sigma, 99.999%) were evaporated from a Knudsen cell onto the monolayer VTe_2, which was kept at 523 K.

XPS measurements

The in situ XPS measurements were performed at the Beijing Synchrotron Radiation Facility. Synchrotron radiation light was monochromated by four high-resolution gratings and controlled by a hemispherical energy analyzer that has photon energy in the range from 10 to 1100 eV.

STEM measurements

Before the STEM measurements, we first deposited 20-nm C_{60} and 80-nm Sb films on the as-grown monolayer J-VTeSe sample in the UHV chamber, aiming to protect the sample from oxidation and damage. Then, the samples were sliced along the SiC (*11*–*20*) face by a focused ion beam and were further thinned to around 40 nm thickness using low-energy ion milling. The cross-sectional high-angle annular dark-field STEM (HAADF-STEM) images were obtained with an aberration-corrected STEM operated at 60 kV. Experimental conditions were as follows: acceleration voltage, 60 kV; beam current, 20 pA; convergence angle, 32 mrad; HAADF collection angle, 75 to 210 mrad; and BF collection angle: 0 to 10 mrad.

Scanning tunneling microscopy measurements

The samples were transferred into the scanning tunneling microscope using a UHV suitcase, with the base pressure of 2×10^{-10} mbar. The STM experiments of the samples were performed at both 300 and 4.5 K. The varying temperature STM measurements were performed under 4.5 K and above 78 K, cooling with liquid helium and liquid nitrogen, respectively. The temperature was controlled by a heater, and the step is ~10 K. All the STM images were measured in constant current mode. All the measurements were performed with the electrochemically etched tungsten tips. The bias voltage was applied to the sample. The tunneling differential conductance (dI/dV) was measured using lock-in detection of the tunnel current by adding a 10-mV modulated bias voltage at 973 Hz of the sample bias voltage.

First-principles calculations

DFT calculations were performed using the generalized gradient approximation for the exchange-correlation potential, the projector augmented wave method (*41*), and a plane-wave basis set as implemented in the Vienna ab initio simulation package (VASP) (*42*). Van der Waals interactions were considered at the DFT-DF level with the optB86b-vdW function (*43*). The finite displacement method implemented in VASP and PHONOPY (*44*) was used to calculate phonon dispersion for the monolayer J-VTeSe. PAW pseudopotentials (V_sv) were used, including V 3 s and 3p semicore states. For the primitive unit cell of monolayer VTe_2, J-VTeSe, and VSe_2, the kinetic energy cutoff for the plane-wave basis set was set to 700 eV for calculating geometric and electronic properties. For supercells, the kinetic energy cutoff was set to 500 eV. A k-mesh of $21 \times 21 \times 1$ was adopted to sample the first Brillouin zone during geometry optimization and the electronic calculations in the unit cell. The k-mesh density was kept in different supercells. The denser k-mesh density of 0.004 $Å^{-1}$ in reciprocal space was used in the 2D Fermi surface calculations. The 2D Fermi surfaces were plotted at the energy range of [$E_F = -30$ meV, $E_F = +30$ meV]. The on-site coulomb interactions were considered on the d orbitals of V atoms with effective value $U = 2.0$ eV and Hund's coupling $J = 0.87$ eV (*45*, *46*) for all configurations. The Fermi surfaces of NM VSe_2 and VTe_2 without Hubbard U match the angle-resolved photoemission spectroscopy measurements above 80 K (*29*, *47*). The electronic properties and phonon spectra of NM pristine structures without Hubbard U were also discussed. All atoms in the supercell were allowed to relax until the residual force per atom was less than 5×10^{-3} eV $Å^{-1}$ and the energy convergence criterion was 1×10^{-5} eV. To consider AFM structures, $2 \times \sqrt{3}$ and $10 \times 3\sqrt{3}$ supercells were adopted to construct pristine and $\sqrt{13} \times \sqrt{13}$ CDW configurations, and the lattice constants of pristine structures were adopted with each magnetic configuration, respectively.

Supplementary Materials

This PDF file includes:

Figs. S1 to S18

Tables S1 and S2

REFERENCES AND NOTES

1. Y. X. Jiang, J. X. Yin, M. M. Denner, N. Shumiya, B. R. Ortiz, G. Xu, Z. Guguchia, J. He, M. S. Hossain, X. Liu, J. Ruff, L. Kautzsch, S. S. Zhang, G. Chang, I. Belopolski, Q. Zhang, T. A. Cochran, D. Multer, M. Litskevich, Z. J. Cheng, X. P. Yang, Z. Wang, R. Thomale, T. Neupert, S. D. Wilson, M. Z. Hasan, Unconventional chiral charge order in kagome superconductor KV_3Sb_5. *Nat. Mater.* **20**, 1353–1357 (2021).
2. Q. Qiao, S. Zhou, J. Tao, J.-C. Zheng, L. Wu, S. T. Ciocys, M. Iavarone, D. J. Srolovitz, G. Karapetrov, Y. Zhu, Anisotropic charge density wave in layered 1*T*-$TiSe_2$. *Phys. Rev. Mater.* **1**, 054002 (2017).
3. M. M. Ugeda, A. J. Bradley, Y. Zhang, S. Onishi, Y. Chen, W. Ruan, C. Ojeda-Aristizabal, H. Ryu, M. T. Edmonds, H.-Z. Tsai, A. Riss, S.-K. Mo, D. Lee, A. Zettl, Z. Hussain, Z.-X. Shen, M. F. Crommie, Characterization of collective ground states in single-layer $NbSe_2$. *Nat. Phys.* **12**, 92–97 (2015).
4. J. Hwang, K. Kim, C. Zhang, T. Zhu, C. Herbig, S. Kim, B. Kim, Y. Zhong, M. Salah, M. M. El-Desoky, C. Hwang, Z. X. Shen, M. F. Crommie, S. K. Mo, Large-gap insulating dimer ground state in monolayer $IrTe_2$. *Nat. Commun.* **13**, 906 (2022).
5. X. Xi, L. Zhao, Z. Wang, H. Berger, L. Forró, J. Shan, K. F. Mak, Strongly enhanced charge-density-wave order in monolayer $NbSe_2$. *Nat. Nanotechnol.* **10**, 765–769 (2015).
6. Y. Hu, T. Zhang, D. Zhao, C. Chen, S. Ding, W. Yang, X. Wang, C. Li, H. Wang, D. Feng, T. Zhang, Real-space observation of incommensurate spin density wave and coexisting charge density wave on Cr (001) surface. *Nat. Commun.* **13**, 445 (2022).
7. X. Xi, Z. Wang, W. Zhao, J.-H. Park, K. T. Law, H. Berger, L. Forró, J. Shan, K. F. Mak, Ising pairing in superconducting $NbSe_2$ atomic layers. *Nat. Phys.* **12**, 139–143 (2015).
8. B. Li, Z. Wan, C. Wang, P. Chen, B. Huang, X. Cheng, Q. Qian, J. Li, Z. Zhang, G. Sun, B. Zhao, H. Ma, R. Wu, Z. Wei, Y. Liu, L. Liao, Y. Ye, Y. Huang, X. Xu, X. Duan, W. Ji, X. Duan, Van der Waals epitaxial growth of air-stable $CrSe_2$ nanosheets with thickness-tunable magnetic order. *Nat. Mater.* **20**, 818–825 (2021).
9. W. Ruan, Y. Chen, S. Tang, J. Hwang, H.-Z. Tsai, R. L. Lee, M. Wu, H. Ryu, S. Kahn, F. Liou, C. Jia, A. Aikawa, C. Hwang, F. Wang, Y. Choi, S. G. Louie, P. A. Lee, Z.-X. Shen, S.-K. Mo, M. F. Crommie, Evidence for quantum spin liquid behaviour in single-layer 1T-$TaSe_2$ from scanning tunnelling microscopy. *Nat. Phys.* **17**, 1154–1161 (2021).
10. Y. Nakata, K. Sugawara, A. Chainani, H. Oka, C. Bao, S. Zhou, P. Y. Chuang, C. M. Cheng, T. Kawakami, Y. Saruta, T. Fukumura, S. Zhou, T. Takahashi, T. Sato, Robust charge-density

wave strengthened by electron correlations in monolayer 1T-$TaSe_2$ and 1T-$NbSe_2$. *Nat. Commun.* **12**, 5873 (2021).
11. Y. Chen, W. Ruan, M. Wu, S. Tang, H. Ryu, H.-Z. Tsai, R. L. Lee, S. Kahn, F. Liou, C. Jia, O. R. Albertini, H. Xiong, T. Jia, Z. Liu, J. A. Sobota, A. Y. Liu, J. E. Moore, Z.-X. Shen, S. G. Louie, S.-K. Mo, M. F. Crommie, Strong correlations and orbital texture in single-layer 1T-$TaSe_2$. *Nat. Phys.* **16**, 218–224 (2020).
12. L. Liu, H. Yang, Y. Huang, X. Song, Q. Zhang, Z. Huang, Y. Hou, Y. Chen, Z. Xu, T. Zhang, X. Wu, J. Sun, Y. Huang, F. Zheng, X. Li, Y. Yao, H. J. Gao, Y. Wang, Direct identification of Mott Hubbard band pattern beyond charge density wave superlattice in monolayer 1T-$NbSe_2$. *Nat. Commun.* **12**, 1978 (2021).
13. L. Du, T. Hasan, A. Castellanos-Gomez, G.-B. Liu, Y. Yao, C. N. Lau, Z. Sun, Engineering symmetry breaking in 2D layered materials. *Nat. Rev. Phys.* **3**, 193–206 (2021).
14. Y. Jiang, X. Lai, K. Watanabe, T. Taniguchi, K. Haule, J. Mao, E. Y. Andrei, Charge order and broken rotational symmetry in magic-angle twisted bilayer graphene. *Nature* **573**, 91–95 (2019).
15. H. Zhao, H. Li, B. R. Ortiz, S. M. L. Teicher, T. Park, M. Ye, Z. Wang, L. Balents, S. D. Wilson, I. Zeljkovic, Cascade of correlated electron states in the kagome superconductor CsV_3Sb_5. *Nature* **599**, 216–221 (2021).
16. W.-M. Zhao, L. Zhu, Z. Nie, Q.-Y. Li, Q.-W. Wang, L.-G. Dou, J.-G. Hu, L. Xian, S. Meng, S.-C. Li, Moiré enhanced charge density wave state in twisted 1T-$TiTe_2$/1T-$TiSe_2$ heterostructures. *Nat. Mater.* **21**, 284–289 (2022).
17. X. Song, L. Liu, Y. Chen, H. Yang, Z. Huang, B. Hou, Y. Hou, X. Han, H. Yang, Q. Zhang, T. Zhang, J. Zhou, Y. Huang, Y. Zhang, H. J. Gao, Y. Wang, Atomic-scale visualization of chiral charge density wave superlattices and their reversible switching. *Nat. Commun.* **13**, 1843 (2022).
18. D. Wu, Y. Ma, Y. Niu, Q. Liu, T. Dong, S. Zhang, J. Niu, H. Zhou, J. Wei, Y. Wang, Z. Zhao, N. Wang, Ultrabroadband photosensitivity from visible to terahertz at room temperature. *Sci. Adv.* **4**, eaao3057 (2018).
19. J. Li, H. Bai, Y. Li, J. Mi, Q. Chen, W. Tang, H. Zhu, X. Fan, Y. Lu, Z. Xu, L. Li, The influence of dimensionality on the charge-density-wave transition and its application on mid-infrared photodetection. *Adv. Opt. Mater.* **11**, 2300720 (2023).
20. I. Vaskivskyi, I. A. Mihailovic, S. Brazovskii, J. Gospodaric, T. Mertelj, D. Svetin, P. Sutar, D. Mihailovic, Fast electronic resistance switching involving hidden charge density wave states. *Nat. Commun.* **7**, 11442 (2016).
21. A. Y. Lu, H. Zhu, J. Xiao, C. P. Chuu, Y. Han, M. H. Chiu, C. C. Cheng, C. W. Yang, K. H. Wei, Y. Yang, Y. Wang, D. Sokaras, D. Nordlund, P. Yang, D. A. Muller, M. Y. Chou, X. Zhang, L. J. Li, Janus monolayers of transition metal dichalcogenides. *Nat. Nanotechnol.* **12**, 744–749 (2017).
22. J. Zhang, S. Jia, I. Kholmanov, L. Dong, D. Er, W. Chen, H. Guo, Z. Jin, V. B. Shenoy, L. Shi, J. Lou, Janus monolayer transition-metal dichalcogenides. *ACS Nano* **11**, 8192–8198 (2017).
23. D. B. Trivedi, G. Turgut, Y. Qin, M. Y. Sayyad, D. Hajra, M. Howell, L. Liu, S. Yang, N. H. Patoary, H. Li, M. M. Petrić, M. Meyer, M. Kremser, M. Barbone, G. Soavi, A. V. Stier, K. Müller, S. Yang, I. S. Esqueda, H. Zhuang, J. J. Finley, S. Tongay, Room-temperature synthesis of 2D Janus crystals and their heterostructures. *Adv. Mater.* **32**, e2006320 (2020).
24. L. Dong, J. Lou, V. B. Shenoy, Large in-plane and vertical piezoelectricity in Janus transition metal dichalchogenides. *ACS Nano* **11**, 8242–8248 (2017).
25. C. Zhang, Y. Nie, S. Sanvito, A. Du, First-principles prediction of a room-temperature ferromagnetic Janus VSSe monolayer with piezoelectricity, ferroelasticity, and large valley polarization. *Nano Lett.* **19**, 1366–1370 (2019).
26. C. Luo, X. Peng, J. Qu, J. Zhong, Valley degree of freedom in ferromagnetic Janus monolayer H-VSSe and the asymmetry-based tuning of the valleytronic properties. *Phys. Rev. B* **101**, 245416 (2020).
27. J. Zhou, W. Zhang, Y.-C. Lin, J. Cao, Y. Zhou, W. Jiang, H. Du, B. Tang, J. Shi, B. Jiang, X. Cao, B. Lin, Q. Fu, C. Zhu, W. Guo, Y. Huang, Y. Yao, S. S. P. Parkin, J. Zhou, Y. Gao, Y. Wang, Y. Hou, Y. Yao, K. Suenaga, X. Wu, Z. Liu, Heterodimensional superlattice with in-plane anomalous Hall effect. *Nature* **609**, 46–51 (2022).
28. M. Bonilla, S. Kolekar, Y. Ma, H. C. Diaz, V. Kalappattil, R. Das, T. Eggers, H. R. Gutierrez, M.-H. Phan, M. Batzill, Strong room-temperature ferromagnetism in VSe_2 monolayers on van der Waals substrates. *Nat. Nanotechnol.* **13**, 289–293 (2018).
29. J. Feng, D. Biswas, A. Rajan, M. D. Watson, F. Mazzola, O. J. Clark, K. Underwood, I. Marković, M. M. Laren, A. Hunter, D. M. Burn, L. B. Duffy, S. Barua, G. Balakrishnan, F. Bertran, P. L. Fèvre, T. K. Kim, G. van der Laan, T. Hesjedal, P. Wahl, P. D. C. King, Electronic structure and enhanced charge-density wave order of monolayer VSe_2. *Nano Lett.* **18**, 4493–4499 (2018).
30. Z.-L. Liu, X. Wu, Y. Shao, J. Qi, Y. Cao, L. Huang, C. Liu, J.-O. Wang, Q. Zheng, Z.-L. Zhu, Epitaxially grown monolayer VSe_2: An air-stable magnetic two-dimensional material with low work function at edges. *Sci. Bull.* **63**, 419–425 (2018).
31. W. Yu, J. Li, T. S. Herng, Z. Wang, X. Zhao, X. Chi, W. Fu, I. Abdelwahab, J. Zhou, J. Dan, Z. Chen, Z. Chen, Z. Li, J. Lu, S. J. Pennycook, Y. P. Feng, J. Ding, K. P. Loh, Chemically exfoliated VSe_2 monolayers with room-temperature ferromagnetism. *Adv. Mater.* **31**, 1903779 (2019).
32. C. van Efferen, J. Berges, J. Hall, E. van Loon, S. Kraus, A. Schobert, T. Wekking, F. Huttmann, E. Plaar, N. Rothenbach, K. Ollefs, L. M. Arruda, N. Brookes, G. Schönhoff, K. Kummer, H. Wende, T. Wehling, T. Michely, A full gap above the Fermi level: The charge density wave of monolayer VS_2. *Nat. Commun.* **12**, 6837 (2021).
33. P. Chen, W. W. Pai, Y. H. Chan, V. Madhavan, M. Y. Chou, S. K. Mo, A. V. Fedorov, T. C. Chiang, Unique gap structure and symmetry of the charge density wave in single-layer VSe_2. *Phys. Rev. Lett.* **121**, 196402 (2018).
34. P. M. Coelho, K. Lasek, K. N. Cong, J. Li, W. Niu, W. Liu, I. I. Oleynik, M. Batzill, Monolayer modification of VTe_2 and its charge density wave. *J. Phys. Chem. Lett.* **10**, 4987–4993 (2019).
35. P. K. J. Wong, W. Zhang, J. Zhou, F. Bussolotti, X. Yin, L. Zhang, A. T. N'Diaye, S. A. Morton, W. Chen, J. Goh, M. P. de Jong, Y. P. Feng, A. T. S. Wee, Metallic 1T phase, $3d^1$ electronic configuration and charge density wave order in molecular beam epitaxy grown monolayer vanadium ditelluride. *ACS Nano* **13**, 12894–12900 (2019).
36. Z.-L. Zhu, Z.-L. Liu, X. Wu, X.-Y. Li, J.-A. Shi, C. Liu, G.-J. Qian, Q. Zheng, L. Huang, X. Lin, J.-O. Wang, H. Chen, W. Zhou, J.-T. Sun, Y.-L. Wang, H.-J. Gao, Charge density wave states in phase-engineered monolayer VTe_2. *Chinese Phys. B* **31**, 077101 (2022).
37. R. Chua, J. Henke, S. Saha, Y. Huang, J. Gou, X. He, T. Das, J. van Wezel, A. Soumyanarayanan, A. T. S. Wee, Coexisting charge-ordered states with distinct driving mechanisms in monolayer VSe_2. *ACS Nano* **16**, 783–791 (2022).
38. J. Pandey, A. Soni, Electron-phonon interactions and two-phonon modes associated with charge density wave in single crystalline 1T-VSe_2. *Phys. Rev. Res.* **2**, 033118 (2020).
39. M. R. Otto, J.-H. Pöhls, L. P. René de Cotret, M. J. Stern, M. Sutton, B. J. Siwick, Mechanisms of electron-phonon coupling unraveled in momentum and time: The case of soft phonons in $TiSe_2$. *Sci. Adv.* **7**, eabf2810 (2021).
40. P. M. Coelho, K. N. Cong, M. Bonilla, S. Kolekar, M.-H. Phan, J. Avila, M. C. Asensio, I. I. Oleynik, M. Batzill, Charge density wave state suppresses ferromagnetic ordering in VSe_2 monolayers. *J. Phys. Chem. C* **123**, 14089–14096 (2019).
41. G. Kresse, D. Joubert, From ultrasoft pseudopotentials to the projector augmented-wave method. *Phys. Rev. B* **59**, 1758–1775 (1999).
42. P. E. Blöchl, Projector augmented-wave method. *Phys. Rev. B* **50**, 17953–17979 (1994).
43. T. Thonhauser, V. R. Cooper, S. Li, A. Puzder, P. Hyldgaard, D. C. Langreth, Van der Waals density functional: Self-consistent potential and the nature of the van der Waals bond. *Phys. Rev. B* **76**, 125112 (2007).
44. A. Togo, I. Tanaka, First principles phonon calculations in materials science. *Scripta Mater.* **108**, 1–5 (2015).
45. H. R. Fuh, C. R. Chang, Y. K. Wang, R. F. Evans, R. W. Chantrell, H. T. Jeng, Newtype single-layer magnetic semiconductor in transition-metal dichalcogenides VX2 (X = S, Se and Te). *Sci. Rep.* **6**, 32625 (2016).
46. S. Kezilebieke, M. N. Huda, P. Dreher, I. Manninen, Y. Zhou, J. Sainio, R. Mansell, M. M. Ugeda, S. van Dijken, H.-P. Komsa, P. Liljeroth, Electronic and magnetic characterization of epitaxial VSe2 monolayers on superconducting NbSe2. *Commun. Phys.* **3**, 116 (2020).
47. B. Rachmilowitz, H. Zhao, H. Li, A. LaFleur, J. Schneeloch, R. Zhong, G. Gu, I. Zeljkovic, Proximity-induced superconductivity in a topological crystalline insulator. *Phys. Rev. B* **100**, 241402 (2019).

Acknowledgments

Funding: The project was funded by the National Key Research and Development Program of China (2022YFA1403500, 2021YFA1400100, and 2023YFA1406500), the National Natural Science Foundation of China (grant nos. 62171035, 62375021, 12374170, 92477205, 52461160327, and 92163206), and the Beijing Nova Program from Beijing Municipal Science and Technology Commission (Z211100002121072). This research benefited from resources and support from the Analysis and Testing Center at the Beijing Institute of Technology. Calculations were performed at the Beijing Super Cloud Computing Center and the Physics Lab of High-Performance Computing of Renmin University of China. C.Z. acknowledged the support from Key Research and Development Program of Wuhan (2024060702030152).

Author contributions: Z.X.: Writing—original draft, conceptualization, investigation, writing—review and editing, methodology, resources, data curation, validation, formal analysis, project administration, and visualization. Y.S.: Conceptualization, investigation, writing—review and editing, resources, validation, and formal analysis. C.H.: Writing—original draft, conceptualization, investigation, writing—review and editing, methodology, data curation, validation, formal analysis, and visualization. C. Zhu: Investigation and formal analysis. G.H.: Investigation and validation. S.H.: Investigation and visualization. Z.-L.L.: Methodology and formal analysis. X.H.: Investigation. Y.H.: Investigation and validation. T.Z.: Investigation. L.L.: Investigation and writing—review and editing. J.-A.S.: Formal analysis. C.L.: Investigation and resources. J.-O.W.: Investigation. W.Z.: Investigation, resources, funding acquisition, and validation. J.Z.: Conceptualization, writing—review and editing, methodology, and supervision. W.J.: Conceptualization, writing—review and editing, methodology, resources, funding acquisition, supervision, formal analysis, and project administration. Y.W.: Conceptualization, investigation, writing—review and editing, methodology, resources, data curation, validation, supervision, formal analysis, software, and visualization. C.Zhang:

Investigation, writing—review and editing, funding acquisition, validation, supervision, and visualization. J.Q.: Writing—original draft, conceptualization, investigation, writing—review and editing, methodology, resources, data curation, validation, supervision, formal analysis, software, project administration, and visualization. H.-J.G.: Resources. X.W.: Writing—original draft, conceptualization, investigation, writing—review and editing, methodology, resources, funding acquisition, data curation, validation, supervision, formal analysis, software, project administration, and visualization. **Competing interests:** The authors declare that they have no competing interests. **Data and materials availability:** All data needed to evaluate the conclusions in the paper are present in the paper and/or the Supplementary Materials.

Submitted 27 May 2024
Accepted 21 May 2025
Published 27 June 2025
10.1126/sciadv.adq4406